Systematic Multi-variable H-infinity Control Design for Primary Frequency Regulation in Stand-alone Microgrids with High Penetration of Renewable Energy Sources

Quang Linh Lam, Antoneta Iuliana Bratcu, Delphine Riu

Systematic Multi-variable $\mathcal{H}_\infty$ Control Design for Primary Frequency Regulation in Stand-Alone Microgrids with High Penetration of Photovoltaic Energy Sources

Quang Linh Lam[1,2], Antoneta Iuliana Bratcu[2] and Delphine Riu[1]

***Abstract*— In this paper, a systematic design of a robust multi-variable control structure for primary frequency regulation in microgrids with high rate of renewable source penetration is proposed. The considered microgrid represents a diesel-photovoltaic-supercapacitor hybrid power generation system operating in stand-alone mode. The proposed control structure relies on a two-level architecture: classical PI-based current tracking controllers are placed on the low control level and receive references from an $\mathcal{H}_\infty$-control-based upper level. A comprehensive methodology that casts the specific engineering demands of microgrid operation into $\mathcal{H}_\infty$ control formalism is detailed. It is also shown how closed-loop dynamical performance requirements must at their turn be taken into account in the initial microgrid setup and sizing, namely in choosing and rating the energy storage system. Numerical simulations carried out in MATLAB®/Simulink® show the effectiveness of the proposed $\mathcal{H}_\infty$ robust control strategy on a MVA-rated microgrid.**

***Index Terms*— Microgrids, primary frequency control, robust control, multi-variable control.**

I. Introduction

The concept of microgrid appears first in the technical literature in [1] and [2] as a promising solution to overcome the challenges of integrating distributed energy resources, including renewable energy sources, into power systems. Microgrid technology allows global reliability to be enhanced, reduction of carbon footprint along with more diversified energy sources, all with smaller investment costs [3].

Reliable operation of microgrids – in either grid-connected or stand-alone mode – claims design of special protection schemes and control systems. From the main grid viewpoint, a microgrid can be seen as a single element responding to appropriate control signals. Such perception goes towards defining microgrids as "energy clusters" that contain loads, Distributed Generation (DG) units and Energy Storage Systems (ESSs) [4].

Stability issues and problems related to low inertia and uncertainties due to presence of renewable energy sources are among the main control challenges [4].

In stand-alone mode it is required to confine the frequency and voltage deviations within a small range to satisfy operating requirements. Presence of high-speed storage systems, such as batteries or supercapacitors, has thus become necessary, leading to new grid configurations that do not longer operate well with conventional control laws. More complex robust control structures are needed to achieve better performance despite uncontrollable disturbances and model uncertainties.

A plethora of control methods have been proposed to handle this kind of problem. Proportional-integral-derivative (PID) control is a widely known and used technique [5], [6]. Despite its intrinsic robustness, this method has limited possibility to ensure satisfactory trade-off among dynamic performances when the operating conditions vary significantly. Fuzzy logic control is proposed in [7]–[9], but it is difficult to obtain a model serving for a systematic control design. $\mathcal{H}_\infty$ control is considered in [10]–[12]; it appears as a powerful tool able to handle multiple requirements in a systematic manner such as to guarantee stability and overall robust performance.

In this paper, the frequency stability problem of microgrids with a high rate of decentralized, renewable and intermittent production is approached. In [13] it is shown that relatively small storage units can significantly reduce frequency deviation, provided that saturation conditions are avoided by dynamically coordinating storage with other generation sources. In this paper a systematic design procedure for computing a multi-variable $\mathcal{H}_\infty$ robust controller for primary frequency regulation is proposed. It is also shown how closed-loop operation demands must at their turn be taken into account in the initial microgrid setup and sizing, namely in appropriately choosing and rating the ESS.

The remainder of this paper is organized as follows. In Section II, microgrid description, coordinated strategy and choice of energy storage technology are presented. Modeling for the $\mathcal{H}_\infty$ control is described in Section III. $\mathcal{H}_\infty$ control design is detailed in Section IV. Numerical simulation results of the proposed control approach is analyzed in Section V. Section VI is dedicated to conclusion and future work.

II. Microgrid Description, Coordinated Strategy and Choice of Energy Storage Technology

A. Microgrid Description

The block diagram of the considered microgrid operating in stand-alone mode is shown in Fig. 1. This microgrid contains a diesel generator as a classical source, a photovoltaic (PV) unit as a renewable source and an energy storage unit. Power sources are connected in parallel to a point of common

[1,2]Q. L. Lam is with Grenoble Institute of Technology; G2Elab, 38031 Grenoble Cedex 1 and GIPSA-lab, 38402 Saint Martin d'Hères Cedex, France Quang-Linh.Lam@g2elab.grenoble-inp.fr

[2]A. I. Bratcu is with Grenoble Institute of Technology; GIPSA-lab Antoneta.Bratcu@gipsa-lab.grenoble-inp.fr

[1]D. Riu is with Grenoble Institute of Technology; G2Elab Delphine.Riu@g2elab.grenoble-inp.fr

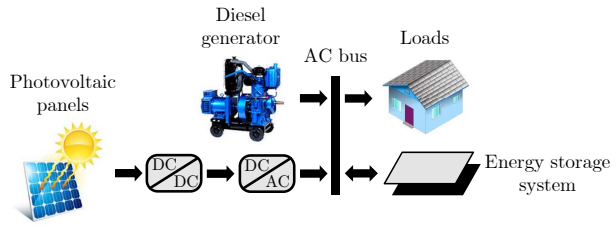

Fig. 1. Block diagram of the studied microgrid.

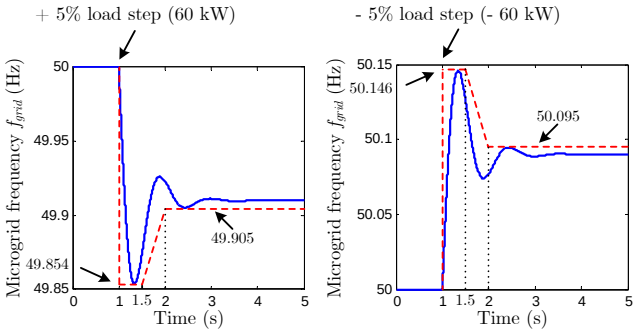

Fig. 2. Performance specification on the microgrid frequency variation in response to a load step of $\pm$ 5% of the rated load power ($\pm$ 60 kW) in the time domain [12].

coupling (PCC) and supply a common load. The bank of PV panels is connected to the PCC through a one-quadrant chopper – inverter which only allows unidirectional power flow, whereas the energy storage system can be operated in charging or discharging mode.

B. Coordinated Strategy

In stand-alone microgrids with high penetration of PV energy sources, the frequency is risky to be unstable or its variations can be considerable and unacceptable [14]. Energy storage systems can then be used to maintain the stability and/or improve the transient response of the frequency in case of disturbances. In the studied microgrid, the proposed coordinated strategy is participation of both the storage system and the diesel generator in primary frequency control. The role of the storage system is to guarantee faster recovery of the microgrid frequency (f_{grid}) consequent to a load power variation, i.e., to improve dynamic performances (overshoot, response time, steady-state error). A template for the frequency variation in response to a step load disturbance of $\pm$ 5% of the rated load power ($\pm$ 60 kW) is shown in Fig. 2; it is defined based on its time-domain response in the case where only the diesel generator participates in primary control [12].

C. Choice of Energy Storage Technology

Energy storage devices can be separated into two different groups with respect to their power supply ability [15]:

- Sources with high power density which are able to supply high power for a short period of time with fast dynamic characteristics, supercapacitors (or ultracapacitors, or electrochemical double-layer capacitors) belong to this class of sources;
- Sources with high energy density which are able to provide power over long periods of time with slow dynamic characteristics, fuel cells and long-time batteries are typical examples of such type of sources.

This classification is illustrated by the Ragone plot [16]. The choice of energy storage technology depends on the desired service. The own frequency f_p (Hz) of each technology of a storage device is determined by $f_p = \rho_p/\rho_e$, where ρ_p (W/kg) and ρ_e (J/kg) are the power density and the energy density of the storage device respectively.

The choice of storage devices for primary frequency control participation is based on analyzing the transfer function between the frequency deviation and the power variation in the frequency domain. The most critical situation of the frequency variation is first studied, then a suitable interval around the critical frequency will be defined for participation of the storage device.

The power variation in the frequency domain $\underline{\Delta P_{diesel}}(s)$, simplified dynamic modeling and frequency control of the diesel generator are expressed by

$$\underline{\Delta P_{diesel}}(s) = -\underbrace{\frac{1}{T_{diesel}s+1}}_{\substack{\text{Simplified dynamic}\\ \text{modeling}}}\underbrace{\left(\underline{K_p}+\frac{\underline{K_i}}{s}\right)}_{\substack{\text{PI controller}\\ \text{for frequency control}}}\underline{\Delta f_{grid}}(s), \tag{1}$$

where the underline denotes per-unitized values. The proportional gain of the PI controller corresponds to primary control, with $\underline{K_p} = 1/\underline{s_{diesel}}$, where $\underline{s_{diesel}}$ is the droop value. The integral gain, $\underline{K_i}$, corresponds to secondary control and is the inverse of the response time of secondary control. T_{diesel} denotes the time constant of the diesel generator.

Without storage device, based on results in [12], [14], [17], [18], the microgrid frequency deviation in the frequency

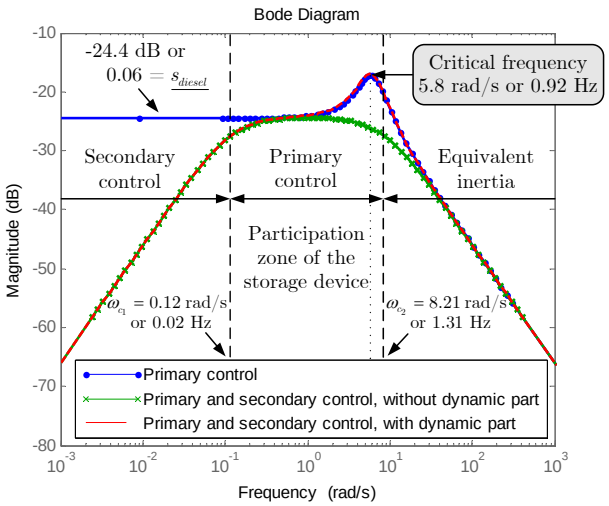

Fig. 3. Bode diagram of the system in (3) with only primary control ($\underline{K_p} \neq 0$, $\underline{K_i} = 0$), both primary and secondary control ($\underline{K_p} \neq 0$, $\underline{K_i} \neq 0$) without the dynamic part of the diesel generator ($T_{diesel} = 0$), both primary and secondary control with the dynamic part ($T_{diesel} \neq 0$).

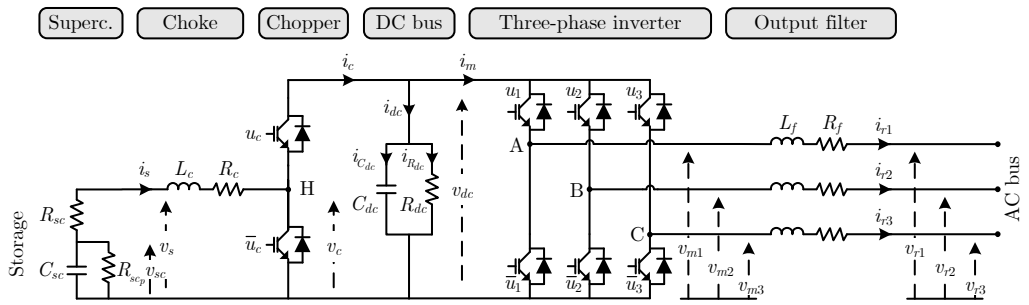

Fig. 4. The full electrical scheme of the energy storage system [12].

domain $\underline{\Delta f_{grid}(s)}$ is given as follows

$$\underline{\Delta f_{grid}}(s) = \frac{\underline{\Delta P_{diesel}}(s) + \overbrace{\underline{\Delta P_{PV}}(s) - \underline{\Delta P_{load}}(s)}^{\underline{\Delta P_{diff}}(s)}}{2\underline{H}s + \underline{D_{load}}}, \quad (2)$$

where $\underline{H}$ is the microgrid equivalent inertia constant and $\underline{D_{load}}$ is the load damping constant.

Substituting (1) into (2) yields

$$\frac{\underline{\Delta f_{grid}}(s)}{\underline{\Delta P_{diff}}(s)} = \frac{(T_{diesel}s+1)\,s}{(2\underline{H}T_{diesel})\,s^3 + \left(2\underline{H} + T_{diesel}\underline{D_{load}}\right)s^2 + \left(\underline{D_{load}} + \underline{K_p}\right)s + \underline{K_i}}. \quad (3)$$

The Bode diagram of the transfer function in (3) is shown in Fig. 3. The system with only primary control can be assumed as a low-pass filter. High-frequency power fluctuations are then filtered by the microgrid equivalent inertia. The DC gain of the transfer function is constant and equal to the droop value $\underline{s_{diesel}}$. Low-frequency power variations are damped by secondary control. The critical frequency value (or resonant frequency) is given in Fig. 3. Power fluctuations around the critical frequency can cause very large frequency variations. Use of a storage device to limit microgrid frequency variations is thus suitable.

Definition of cut-off frequencies to separate frequency intervals would be useful to define participation bandwidth of the storage device, which is then applied for choosing appropriate storage technology. In order to calculate these cut-off frequencies, the dynamic part of the diesel generator is firstly neglected (i.e., $T_{diesel} = 0$) to simplify the expression of the transfer function given in (3) as follows

$$\frac{\underline{\Delta f_{grid}}(s)}{\underline{\Delta P_{diff}}(s)} = \frac{s/\underline{K_i}}{\frac{2\underline{H}}{\underline{K_i}}s^2 + \frac{\underline{D_{load}}+\underline{K_p}}{\underline{K_i}}s + 1}, \quad (4)$$

which corresponds to a second-order system with a zero at the origin, the corner frequency $\omega_n = \sqrt{\underline{K_i}/2\underline{H}}$ and the damping ratio $\zeta = \left(\underline{D_{load}} + \underline{K_p}\right)\Big/\left(2\sqrt{2\underline{H}\underline{K_i}}\right)$. The magnitude of this transfer function is illustrated in Fig. 3. For the considered microgrid, ζ is equal to 4.17, therefore, two cut-off frequencies denoted $\omega_{c_{1,2}}$ can be calculated as

$$\omega_{c_{1,2}} = \frac{1}{4\underline{H}}\left|-\left(\underline{D_{load}} + \underline{K_p}\right) \pm \sqrt{\left(\underline{D_{load}} + \underline{K_p}\right)^2 - 8\underline{H}\underline{K_i}}\right|. \quad (5)$$

Substituting microgrid parameter values into (5) gives the low cut-off frequency $\omega_{c_1} = 0.12$ rad/s (or $f_{c_1} = 0.02$ Hz) and the high cut-off frequency $\omega_{c_2} = 8.21$ rad/s (or $f_{c_2} = 1.31$ Hz). Moreover, as analyzed in Fig. 3, the dynamic part affects the medium-frequency region which corresponds to primary control and it hardly affects cut-off frequencies. Hence, the frequency interval $f_c \in [0.02, 1.31]$ Hz is chosen for primary control participation of the storage device. By comparing this frequency interval with the own frequency of each storage technology deduced from the Ragone plot in [16], one can conclude that **supercapacitor storage technology** with its own frequency $f_p \in [0.00278, 27.78]$ Hz is the most appropriate one and consequently selected for primary control participation.

The supercapacitor power source is connected to the PCC and controlled by means of a two-quadrant chopper – inverter which allows bidirectional power flow. The full electrical scheme of the storage system is presented in Fig. 4 [12]. Another control objective which must be taken into account is to regulate the DC-bus voltage (v_{dc}) at the desired value of 1000 V. This performance specification (Fig. 5), relied on the one proposed recently in [12]. By imposing suitable small-signal performances, large-signal standards can be guaranteed.

III. Modeling for $\mathcal{H}_\infty$ Control

In this paper, the energy storage system is modeled by using the averaged modeling. The non-linear averaged model is obtained from its topological model [19]. By linearizing the non-linear averaged model around an equilibrium point supposing that the PCC voltages in d–axis and q–axis respectively (v_{rd}, v_{rq}) remain constant (i.e., $\Delta v_{rd} = 0$, $\Delta v_{rq} = 0$), the linear averaged model is obtained in [12].

In some cases, for instance, $\mathcal{H}_\infty$ control design, it is often more convenient to express a power-electronic converter system in a per-unit term. For the considered storage system, the base values for AC-side quantities are given in Appendix. The DC-side base values are determined based on those of the AC side [20] and summarized in Appendix. Let us note a

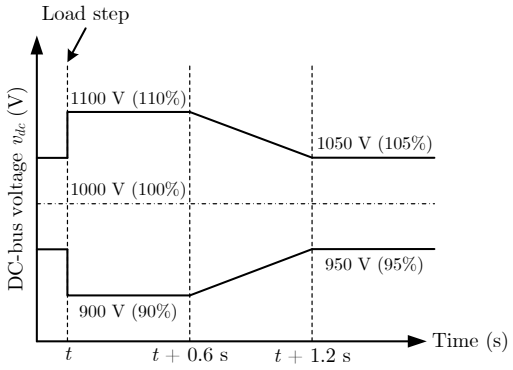

Fig. 5. Performance specification on the DC-bus voltage variation in response to a load step in the time domain.

per-unitized value by the underline, then the linear averaged model of the storage system is described by the following per-unitized set of equations

$$\frac{1}{\omega_b}\frac{d\underline{\Delta v_{sc}}}{dt} = -\frac{1}{\underline{C_{sc}}}\underline{\Delta i_s} - \frac{1}{\underline{R_{sc_p}}\underline{C_{sc}}}\underline{\Delta v_{sc}}, \tag{6}$$

$$\begin{aligned}\frac{1}{\omega_b}\frac{d\underline{\Delta v_{dc}}}{dt} = {} & \frac{1}{\underline{C_{dc}}}\alpha_{c_e}\underline{\Delta i_s} + \frac{1}{\underline{C_{dc}}}\underline{i_{s_e}}\Delta\alpha_c - \frac{1}{\underline{C_{dc}}}\Big(\beta_{d_e}\underline{\Delta i_{rd}} \\ & + \underline{i_{rd_e}}\Delta\beta_d + \beta_{q_e}\underline{\Delta i_{rq}} + \underline{i_{rq_e}}\Delta\beta_q\Big) \\ & - \frac{1}{\underline{R_{dc}}\underline{C_{dc}}}\underline{\Delta v_{dc}},\end{aligned} \tag{7}$$

$$\begin{aligned}\frac{1}{\omega_b}\frac{d\underline{\Delta i_s}}{dt} = {} & \frac{1}{\underline{L_c}}\underline{\Delta v_{sc}} - \frac{\underline{R_{sc}} + \underline{R_c}}{\underline{L_c}}\underline{\Delta i_s} \\ & - \frac{1}{\underline{L_c}}\alpha_{c_e}\underline{\Delta v_{dc}} - \frac{1}{\underline{L_c}}\underline{v_{dc_e}}\Delta\alpha_c,\end{aligned} \tag{8}$$

$$\begin{aligned}\frac{1}{\omega_b}\frac{d\underline{\Delta i_{rd}}}{dt} = {} & \frac{1}{\underline{L_f}}\beta_{d_e}\underline{\Delta v_{dc}} + \frac{1}{\underline{L_f}}\underline{v_{dc_e}}\Delta\beta_d - \frac{\underline{R_f}}{\underline{L_f}}\underline{\Delta i_{rd}} \\ & + \underline{\omega_{grid_e}}\underline{\Delta i_{rq}} + \underline{i_{rq_e}}\Delta\underline{\omega_{grid}},\end{aligned} \tag{9}$$

$$\begin{aligned}\frac{1}{\omega_b}\frac{d\underline{\Delta i_{rq}}}{dt} = {} & \frac{1}{\underline{L_f}}\beta_{q_e}\underline{\Delta v_{dc}} + \frac{1}{\underline{L_f}}\underline{v_{dc_e}}\Delta\beta_q - \frac{\underline{R_f}}{\underline{L_f}}\underline{\Delta i_{rq}} \\ & - \underline{\omega_{grid_e}}\underline{\Delta i_{rd}} - \underline{i_{rd_e}}\Delta\underline{\omega_{grid}},\end{aligned} \tag{10}$$

where the state variables are: the supercapacitor voltage ($\underline{\Delta v_{sc}}$), the DC-bus voltage ($\underline{\Delta v_{dc}}$), the storage device current ($\underline{\Delta i_s}$) and the inverter output currents in d–axis and q–axis respectively ($\underline{\Delta i_{rd}}$, $\underline{\Delta i_{rq}}$). α_c is the average value of the chopper switching function, β_d and β_q are the average values of the inverter switching functions in d–axis and q–axis respectively, $\underline{\omega_{grid}}$ is the microgrid pulsation.

The power variation of diesel generation in the time domain ($\underline{\Delta P_{diesel}}$) for only primary control participation (i.e., $\underline{K_p} \neq 0$, $\underline{K_i} = 0$) is obtained by applying the inverse Laplace transform to (1)

$$\frac{d\underline{\Delta P_{diesel}}}{dt} = -\frac{1}{T_{diesel}}\underline{\Delta P_{diesel}} - \frac{1}{T_{diesel}\underline{s_{diesel}}}\underline{\Delta f_{grid}}. \tag{11}$$

Based on results in [12], [14], [17], [18] and supposing that PV source power is constant (i.e., $\underline{\Delta P_{PV}} = 0$), the per-unitized equation expressing the microgrid frequency deviation in the time domain $\underline{\Delta f_{grid}}$ is written as

$$\begin{aligned}\frac{d\underline{\Delta f_{grid}}}{dt} = {} & \frac{1}{2\underline{H}}\Big[\underline{i_{s_e}}\underline{\Delta v_{sc}} + \Big(\underline{v_{sc_e}} - 2\underline{R_{sc}}\underline{i_{s_e}}\Big)\underline{\Delta i_s} \\ & + \underline{\Delta P_{diesel}} - \underline{\Delta P_{load}}\Big] - \frac{\underline{D_{load}}}{2\underline{H}}\underline{\Delta f_{grid}}.\end{aligned} \tag{12}$$

Subscript e indicates the steady-state equilibrium point. Steady-state real-unit values are given in Table I.

TABLE I
STEADY-STATE REAL-UNIT VALUES OF THE LINEAR SYSTEM

Variable	v_{sc_e}	v_{dc_e}	v_{rd_e}	v_{rq_e}	i_{s_e}
Value	780 V	1000 V	400 V	0 V	−3.4 A
Variable	i_{rd_e}	i_{rq_e}	α_{c_e}	β_{d_e}	β_{q_e}
Value	−21.6 A	0 A	0.78	0.4	−0.003
Variable	P_{diesel_e}	P_{PV_e}	P_{load_e}	f_{grid_e}	ω_{grid_e}
Value	1.0026 MW	0.2 MW	1.2 MW	50 Hz	100π rad/s

IV. $\mathcal{H}_\infty$ CONTROL DESIGN

This section details the control approach used to achieve the control objectives previously mentioned in Section II. Its basic idea is to consider the current variations $\underline{\Delta i_s}$ and $\underline{\Delta i_{rd}}$ as control inputs for the linearized system (6), (7), (11) and (12), which should result from the disturbance rejection requirement $\underline{\Delta P_{load}}$. The global control structure is illustrated in Fig. 6, where control loops are separated into two cascaded levels.

A. Current Control Level

The current variations Δi_s, Δi_{rd} and Δi_{rq} must be controlled and prevented from exceeding admissible limits. All current control loops have fast closed-loop dynamics compared to the $\mathcal{H}_\infty$ control loop, therefore, they are grouped together.

$\underline{\Delta i_{rq}}$ (or Δi_{rq}) in (9) is considered a high-frequency perturbation, which is further significantly reduced by the $d-q$ decoupling structure. The same applies for $\underline{\Delta i_{rd}}$ (or Δi_{rd}) in (10). $\underline{\Delta v_{dc}}$ (or Δv_{dc}) and $\underline{\Delta\omega_{grid}}$ (or $\Delta\omega_{grid}$) in (8), (9), (10) are regarded as low-frequency perturbations that are rejected by the upper-level control. Hence, the transfer functions relating the current variations with the duty ratio variations (inner plants) are computed straightforwardly from (8), (9) and (10)

$$G_{i_s-\alpha_c}(s) = \frac{\Delta i_s(s)}{\Delta\alpha_c(s)} = \frac{K_s}{T_s s + 1}, \tag{13}$$

$$G_{i_{rdq}-\beta_{dq}}(s) = \frac{\Delta i_{rd}(s)}{\Delta\beta_d(s)} = \frac{\Delta i_{rq}(s)}{\Delta\beta_q(s)} = \frac{K_{rdq}}{T_{rdq}s + 1}, \tag{14}$$

where $K_s = -v_{dc_e}/(R_{sc} + R_c)$, $T_s = L_c/(R_{sc} + R_c)$, $K_{rdq} = v_{dc_e}/R_f$ and $T_{rdq} = L_f/R_f$.

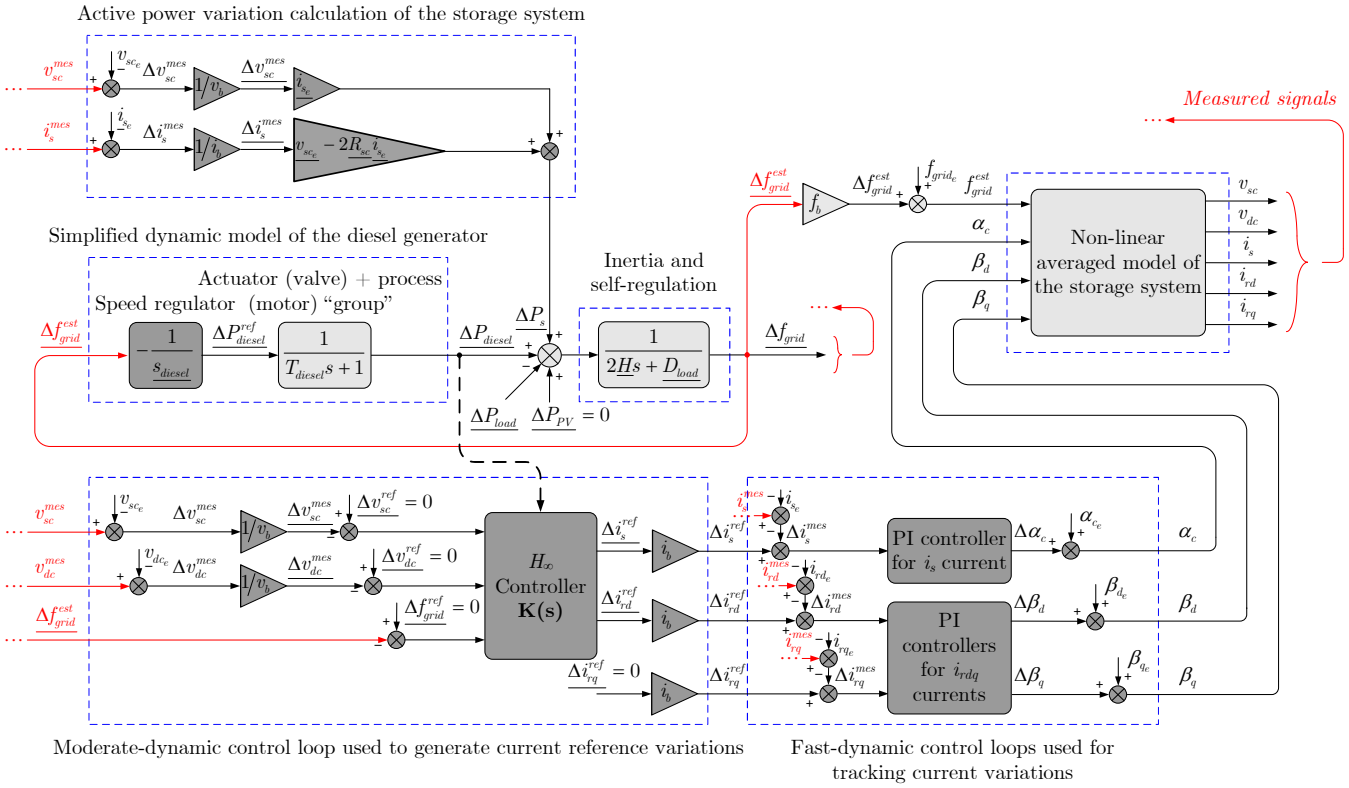

Fig. 6. Block diagram of the proposed global control structure.

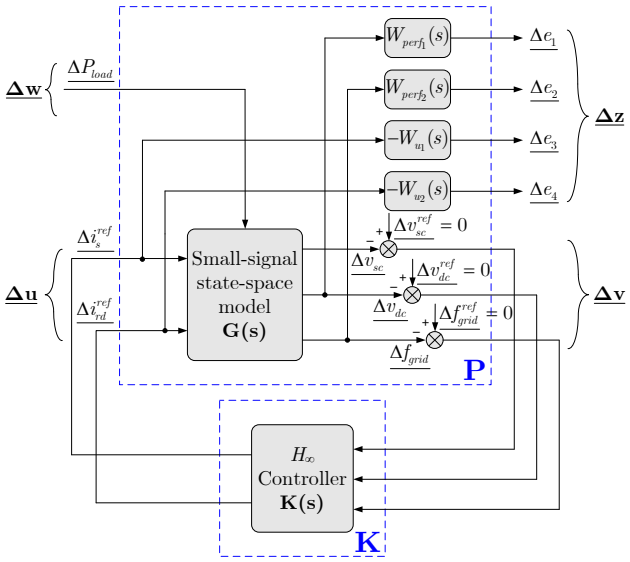

Fig. 7. Control configuration in the so-called $\mathbf{P}-\mathbf{K}$ form, where $\mathbf{P}$ denotes the plant together with the weighting functions and $\mathbf{K}$ denotes the $\mathcal{H}_\infty$ controller.

Because the inner plants are of first order, PI controllers of the form $G_{PI}(s) = K_p\left(1+\frac{1}{T_i s}\right)$ are effectively used to ensure both the zero steady-state error and the desired closed-loop bandwidth. Current reference variations Δi_s^{ref} and Δi_{rd}^{ref} are generated by the outer $\mathcal{H}_\infty$ control loop, whereas $\Delta i_{rq}^{ref} = 0$ (reactive power reference variation ΔQ_s^{ref} of the storage system is assumed to be equal to 0, therefore, $\Delta i_{rq}^{ref} = -\Delta Q_s^{ref}/v_{rd_e} = 0$). Prefilters $G_{pf_s}(s) = 1/(T_{i_s}s+1)$ and $G_{pf_{rdq}}(s) = 1/\left(T_{i_{rdq}}s+1\right)$ must also be inserted to cancel the inner closed-loop zeros.

Let the inner closed-loop dynamical performance be described by the bandwidth $1/T_0$ and the damping coefficient ζ_0. In our case study, we impose the closed-loop dynamics ten times faster than the original current plants, $T_{0_s} = T_s/10 = 11.4$ ms, $T_{0_{rdq}} = T_{rdq}/10 = 9.6$ ms and the damping ratios $\zeta_{0_s} = \zeta_{0_{rdq}} = 0.8$.

B. $\mathcal{H}_\infty$ Control Level

The current variations Δi_s and Δi_{rd} are controlled by the very fast-dynamic loops which satisfy tracking of all current reference variations generated by the $\mathcal{H}_\infty$ controller, therefore, the outer $\mathcal{H}_\infty$ plant "sees" $\Delta i_s \equiv \Delta i_s^{ref}$ and $\Delta i_{rd} \equiv \Delta i_{rd}^{ref}$. The linearized system (6), (7), (11) and (12) is represented in the state-space form as follows (with the terms $\frac{1}{C_{dc}} i_{s_e} \Delta\alpha_c$, $\frac{1}{C_{dc}} i_{rd_e} \Delta\beta_d$ and $\frac{1}{C_{dc}} i_{rq_e} \Delta\beta_q$ in (7) being neglected in the outer $\mathcal{H}_\infty$ control loop design, $\underline{\Delta i_{rq}} = \underline{\Delta i_{rq}^{ref}} = 0$)

$$\begin{cases} \underline{\mathbf{\Delta \dot{x}}} = \mathbf{A}\underline{\mathbf{\Delta x}} + \mathbf{B_1}\underline{\mathbf{\Delta u}} + \mathbf{B_2}\underline{\mathbf{\Delta w}} \\ \underline{\mathbf{\Delta y}} = \mathbf{C}\underline{\mathbf{\Delta x}} + \mathbf{D_1}\underline{\mathbf{\Delta u}} + \mathbf{D_2}\underline{\mathbf{\Delta w}} \end{cases}, \tag{15}$$

where $\underline{\mathbf{\Delta x}} = \left[\begin{array}{cccc} \underline{\Delta v_{sc}} & \underline{\Delta v_{dc}} & \underline{\Delta P_{diesel}} & \underline{\Delta f_{grid}} \end{array}\right]^T$ is the state vector, $\underline{\mathbf{\Delta u}} = \left[\begin{array}{cc} \underline{\Delta i_s^{ref}} & \underline{\Delta i_{rd}^{ref}} \end{array}\right]^T$ is the control input vector, $\underline{\mathbf{\Delta w}} = \underline{\Delta P_{load}}$ is the load power variation, which represents the disturbance input, and $\underline{\mathbf{\Delta y}} =$

$\left[\ \underline{\Delta v_{sc}}\ \ \underline{\Delta v_{dc}}\ \ \underline{\Delta f_{grid}}\ \right]^T$ is the measured output vector. Matrices $\mathbf{A}$, $\mathbf{B_1}$, $\mathbf{B_2}$, $\mathbf{C}$, $\mathbf{D_1}$ and $\mathbf{D_2}$ are given in Appendix.

The multi-variable $\mathcal{H}_\infty$ control formulation proposed in Fig. 7 is afforded by the general control configuration in [21]. In our case study, focus is on the disturbance rejection problem corresponding to the load power variation, therefore, the S/KS mixed-sensitivity optimization must typically be solved [21]. This design method requires definition of frequency weights $W_{perf}(s)$ to formalize the disturbance rejection objectives (performance specifications) and frequency weights $W_u(s)$ to translate the practical implementation constraints of the control inputs.

The generalized plant $\mathbf{P}$ has three inputs, namely, the load power variation $\underline{\Delta P_{load}}$ acting as a disturbance input $\underline{\mathbf{\Delta w}}$ and the current reference variations $\underline{\Delta i_s^{ref}}$, $\underline{\Delta i_{rd}^{ref}}$ which are the control inputs $\underline{\mathbf{\Delta u}}$. The output vector, $\underline{\mathbf{\Delta y}}$, is composed of the supercapacitor voltage variation $\underline{\Delta v_{sc}}$, the DC-bus voltage variation $\underline{\Delta v_{dc}}$ and the frequency variation $\underline{\Delta f_{grid}}$.

Weighting functions selection is the key to cope with the performance requirements. The DC-bus voltage variation and the frequency variation are bounded by first-order weighting functions $W_{perf}(s)$ of the following form [21]

$$\frac{1}{W_{perf}(s)} = \frac{s + \omega_b A_\varepsilon}{s/M_s + \omega_b}. \tag{16}$$

The function $1/W_{perf}(s)$ can be representative of time-domain response specifications, where the high-frequency gain M_s has an influence on the system overshoot, the cut-off frequency ω_b tunes the desired response time and the low-frequency gain A_ε allows limiting the steady-state error.

The first weighting function $W_{perf_1}(s)$ is designed for $\underline{\Delta v_{dc}}$ to impose a bandwidth forty times smaller than the $\underline{\Delta i_{rd}}$ inner closed-loop one, $\omega_{b_1} = 1/\left(40T_{0_{rdq}}\right) = 2.61$ rad/s (or a response time of approximately $t_{r_1} \approx 1.2$ s). $M_{s_1} = \left(0.01\underline{v_{dc_e}}\right)\Big/\left(0.05\underline{P_{load_e}}\right) = 0.833$ is chosen to limit a maximum overshoot of 1% of the rated DC-bus voltage (10 V) in response to a load step of 5% of the rated load power. Similarly, one imposes $A_{\varepsilon_1} = \left(0.005\underline{v_{dc_e}}\right)\Big/\left(0.05\underline{P_{load_e}}\right) = 0.417$ to ensure a desired steady-state error being less than or equal to 0.5% of the rated DC-bus voltage (5 V).

The parameters of the second weighting function $W_{perf_2}(s)$ designed for $\underline{\Delta f_{grid}}$ are chosen to improve the transient response of the frequency compared to its performance specification in Fig. 2. $\omega_{b_2} = 2\omega_{b_1} = 5.22$ rad/s is chosen to ensure a response time of approximately $t_{r_2} \approx 0.6$ s. Imposing $M_{s_2} = [(50.12 - 50)/f_b]\Big/\left(0.05\underline{P_{load_e}}\right) = 0.08$ allows limiting a maximum frequency overshoot of 0.12 Hz in response to a load step of 5% of the rated load power. $A_{\varepsilon_2} = [(50.06 - 50)/f_b]\Big/\left(0.05\underline{P_{load_e}}\right) = 0.04$ is chosen to ensure a desired steady-state error being less than or equal to 0.06 Hz.

As analyzed in Section II, the frequency interval $f_c \in [0.02, 1.31]$ Hz (or $\omega_c \in [0.12, 8.21]$ rad/s) was selected for primary control participation of the storage device. Moreover, the active power injection or absorption of the storage system is controlled via i_s. Thus, the storage device current reference variation $\underline{\Delta i_s^{ref}}$ is bounded by a band-pass weighting function $W_{u_1}(s)$ written as follows

$$\frac{1}{W_{u_1}(s)} = A_{u_1}\frac{\left(\frac{M_{u_1}}{\omega_{bc_{11}}}s+1\right)\left(\frac{A_{u_1}}{\omega_{bc_{12}}}s+1\right)}{\left(\frac{A_{u_1}}{\omega_{bc_{11}}}s+1\right)\left(\frac{M_{u_1}}{\omega_{bc_{12}}}s+1\right)}, \frac{\omega_{bc_{11}}}{A_{u_1}} < \frac{\omega_{bc_{12}}}{M_{u_1}}. \tag{17}$$

$M_{u_1} = \left(\underline{i_{s_{max}}} - \underline{i_{s_e}}\right)\Big/\left(0.05\underline{P_{load_e}}\right) = 9.62$ is chosen to prevent the storage device current reference from exceeding its admissible limit $i_{s_{max}}$ consequent to a load step of 5% of the rated load power. A small value of $A_{u_1} = 0.1M_{u_1} = 0.962$ is imposed. In our case study, the own frequency of the selected supercapacitor technology is $f_p = 0.48$ Hz ($\omega_p = 3.04$ rad/s), therefore, one chooses $\omega_{bc_{11}}/A_{u_1} = 3.04$ rad/s resulting in $\omega_{bc_{11}} = 2.93$ rad/s. Additionally, $\omega_{bc_{12}}/M_{u_1} = \omega_{c_{max}} = 8.21$ rad/s is chosen, which leads to $\omega_{bc_{12}} = 78.98$ rad/s.

The DC-bus voltage is regulated via i_{rd}. The inverter output current reference variation in d–axis $\underline{\Delta i_{rd}^{ref}}$ is bounded by the following first-order weighting function [21]

$$\frac{1}{W_{u_2}(s)} = \frac{A_{u_2}s + \omega_{bc_2}}{s + \omega_{bc_2}/M_{u_2}}. \tag{18}$$

$M_{u_2} = \left(\underline{i_{rd_{max}}} - \underline{i_{rd_e}}\right)\Big/\left(0.05\underline{P_{load_e}}\right) = 8.48$ is imposed to limit the current reference below its maximum value $i_{rd_{max}}$ consequent to a load step of 5% of the rated load power. A small value of $A_{u_2} = 0.1M_{u_2} = 0.848$ is chosen. $\omega_{bc_2} = 1/(100T_{s_i}) = 40$ rad/s, where $T_{s_i} = 1/f_{s_i}$, is chosen to impose a bandwidth one hundred times smaller than the inverter switching frequency f_{s_i}.

According to the system modeling and the selected weighting functions, a full-order $\mathcal{H}_\infty$ controller is designed using the MATLAB® software environment. The obtained result corresponds to the minimization of the norm

$$\left\| \begin{array}{c} W_{perf}S \\ W_uKS \end{array} \right\|_\infty < \gamma, \tag{19}$$

where the sensitivity functions are defined as follows

$$S_1 = \frac{\underline{\Delta v_{dc}}}{\underline{\Delta P_{load}}}, S_2 = \frac{\underline{\Delta f_{grid}}}{\underline{\Delta P_{load}}}, \tag{20}$$

$$KS_1 = \frac{\underline{\Delta i_s^{ref}}}{\underline{\Delta P_{load}}}, KS_2 = \frac{\underline{\Delta i_{rd}^{ref}}}{\underline{\Delta P_{load}}}. \tag{21}$$

Design procedure may yield unstable controllers. In this case, the value γ_{min} must be slightly increased to reduce the constraint on the control and result in stable controllers. The full-order $\mathcal{H}_\infty$ controller found has 9 states with a conditioning value of $\gamma = 169.83$.

In summary, the systematic procedure for $\mathcal{H}_\infty$ control design can be carried out as follows

- **Step 1:** Analyzing the transfer function between frequency deviation and power variation in the frequency domain, then computing a suitable frequency interval for storage device participation in primary frequency

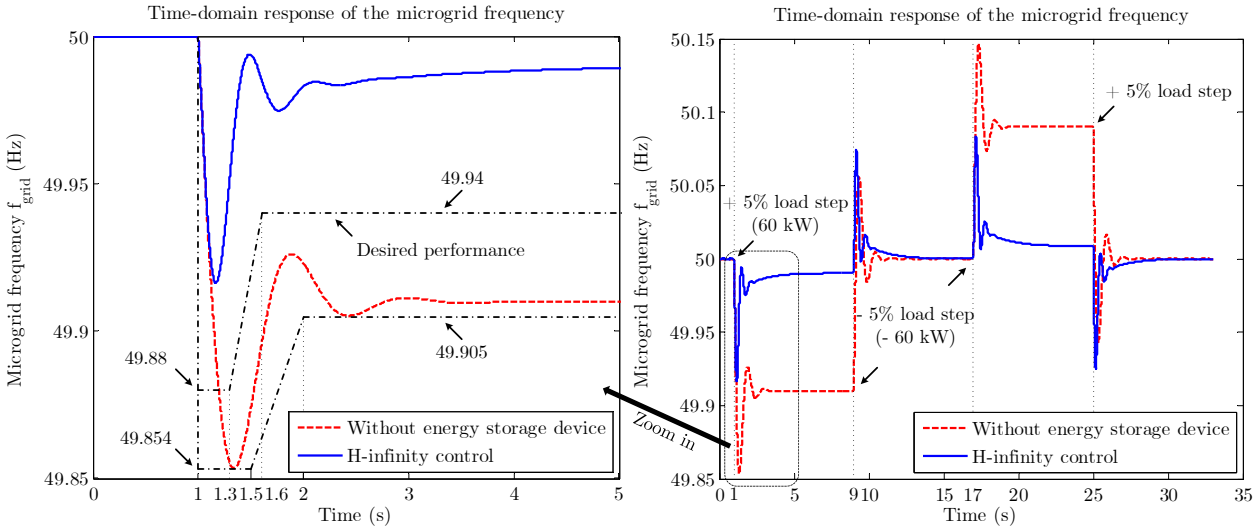

Fig. 8. Time-domain response of the microgrid frequency f_{grid} under small step load disturbances of $\pm$ 5% of the rated load power ($\pm$ 60 kW).

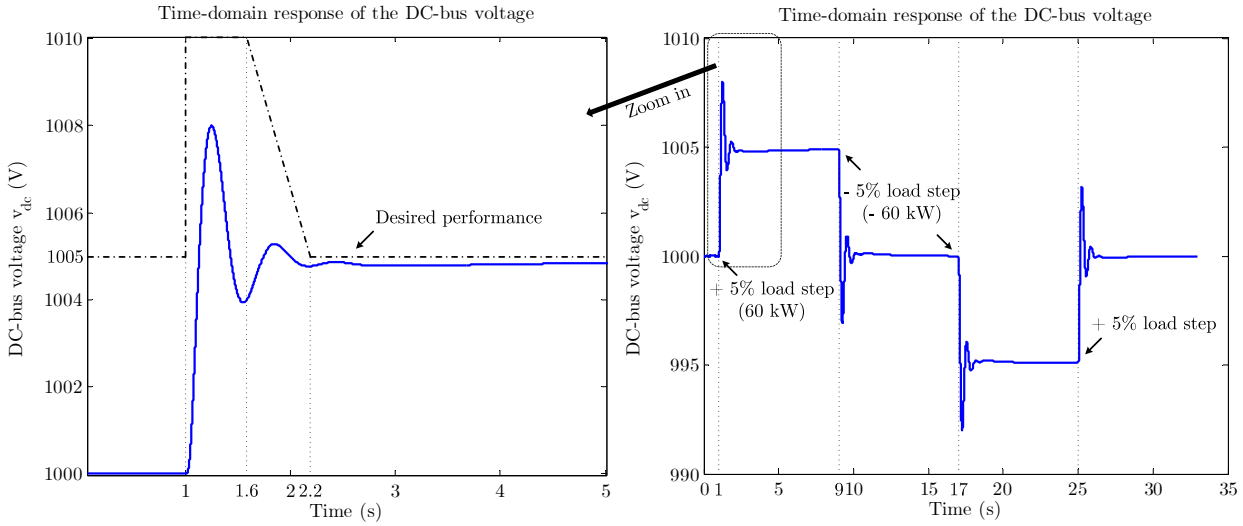

Fig. 9. Time-domain response of the DC-bus voltage v_{dc} under small step load disturbances of $\pm$ 5% of the rated load power ($\pm$ 60 kW).

control and choosing a storage technology which is the most appropriate to this frequency interval;

- **Step 2:** System modeling and casting the specific engineering demands of microgrid operation into $\mathcal{H}_\infty$ control formalism;
- **Step 3:** Selecting the weighting functions according to control objectives and control input constraints;
- **Step 4:** Synthesizing an $\mathcal{H}_\infty$ controller and performing numerical simulations to verify if the control objectives are satisfied or not. If not, go to Step 3.

V. Numerical Simulation Results

Numerical simulations under MATLAB®/Simulink® are performed to show the effectiveness of the proposed control approach. The non-linear averaged model is used for the time-domain simulations. The load profile is varied in step of + 5% of the rated load power (60 kW) at $t = 1$ s, − 5% at $t = 9$ s, − 5% at $t = 17$ s and + 5% at $t = 25$ s.

Fig. 8 presents the time-domain response of the microgrid frequency. One can see that the desired time-domain performance corresponding to the parameter choice of the weighting function $W_{perf_2}(s)$ in Section IV is well-respected. Primary frequency control participation of the storage device has allowed improving significantly the dynamic performances (i.e., lower overshoot, faster response time, smaller steady-state error) compared with the case where only the diesel generator participates in primary control. Fig. 9 shows that the DC-bus voltage control objective is satisfied with respect to the parameter selection of the weighting function $W_{perf_1}(s)$ in Section IV (the desired time-domain performance is met). Therefore, the proposed $\mathcal{H}_\infty$ controller ensures the desired performance specifications. The time-domain responses of the energy storage device current and the inverter output current in d–axis are given in Fig. 10.

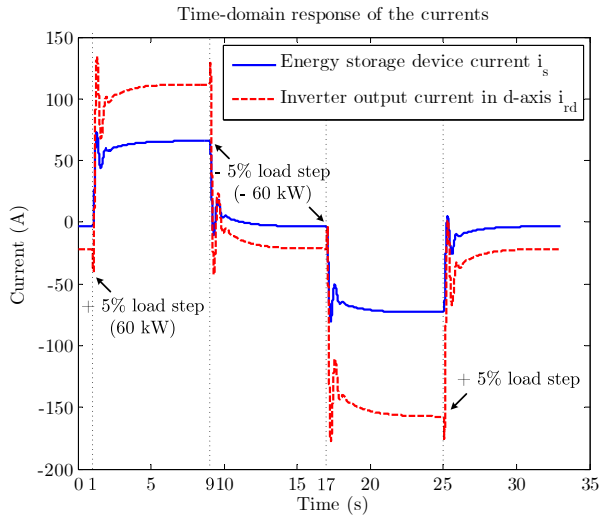

Fig. 10. Time-domain response of the energy storage device current i_s and the inverter output current in d–axis i_{rd} under small step load disturbances of $\pm$ 5% of the rated load power ($\pm$ 60 kW).

VI. Conclusion and Future Work

This paper has presented a systematic design procedure for computing a multi-variable $\mathcal{H}_\infty$ robust controller for primary frequency regulation in stand-alone microgrids highly penetrated by renewable energy sources. Effectiveness of the proposed $\mathcal{H}_\infty$ robust control strategy has been validated via numerical simulation results. Future work can concern robustness analysis of the synthesized $\mathcal{H}_\infty$ controller taking into account power output variation of the PV source. Use of Linear Parameter Varying (LPV) control will also be envisaged to ensure good performance if the synthesized $\mathcal{H}_\infty$ controller is not robust to significant variations of the operating point (storage system capacity, PV power output,...). The next main prospect of this paper is to design a robust control strategy for PCC voltage regulation. Practical implementation of the proposed control algorithms on a real-time test bench must also be envisaged.

Appendix

Matrices in the small-signal state-space model for the $\mathcal{H}_\infty$ control level

$$\mathbf{A} = \begin{bmatrix} -\frac{\omega_b}{R_{sc_p}C_{sc}} & 0 & 0 & 0 \\ 0 & -\frac{\omega_b}{R_{dc}C_{dc}} & 0 & 0 \\ 0 & 0 & -\frac{1}{T_{diesel}} & -\frac{1}{T_{diesel}s_{diesel}} \\ \frac{1}{2\underline{H}}\underline{i_{s_e}} & 0 & \frac{1}{2\underline{H}} & -\frac{\underline{D_{load}}}{2\underline{H}} \end{bmatrix}$$

$$\mathbf{B_1} = \begin{bmatrix} -\frac{\omega_b}{C_{sc}} & 0 \\ \frac{\omega_b}{C_{dc}}\alpha_{c_e} & -\frac{\omega_b}{C_{dc}}\beta_{d_e} \\ 0 & 0 \\ \frac{1}{2\underline{H}}\left(\underline{v_{sc_e}} - 2\underline{R_{sc}}\underline{i_{s_e}}\right) & 0 \end{bmatrix}, \mathbf{B_2} = \begin{bmatrix} 0 \\ 0 \\ 0 \\ -\frac{1}{2\underline{H}} \end{bmatrix}$$

$$\mathbf{C} = \begin{bmatrix} 1 & 0 & 0 & 0 \\ 0 & 1 & 0 & 0 \\ 0 & 0 & 0 & 1 \end{bmatrix}, \mathbf{D_1} = \begin{bmatrix} 0 & 0 \\ 0 & 0 \\ 0 & 0 \end{bmatrix}, \mathbf{D_2} = \begin{bmatrix} 0 \\ 0 \\ 0 \end{bmatrix}.$$

References

[1] B. Lasseter, "Microgrids [distributed power generation]," in *Proc. IEEE Power Eng. Soc. Winter Meet.*, vol. 1, pp. 146–149, Jan. 2001.

[2] R. H. Lasseter, "Microgrids," in *Proc. IEEE Power Eng. Soc. Winter Meet.*, vol. 1, pp. 305–308, Jan. 2002.

[3] U. S. Department of Energy. (2008) The smart grid: An introduction. [Online]. Available: http://www.energy.gov/oe/downloads/smart-grid-introduction

[4] D. E. Olivares *et al.*, "Trends in microgrid control," *IEEE Trans. Smart Grid*, vol. 5, no. 4, pp. 1905–1919, Jul. 2014.

[5] B. Dong, Y. Li, and Z. Zheng, "Control strategies of DC-bus voltage in islanded operation of microgrid," in *Proc. 4th Int. Conf. Electric Utility Deregulation Restructuring Power Technologies*, pp. 1671–1674, Jul. 2011.

[6] V. S. Sundaram and T. Jayabarathi, "Load frequency control using PID tuned ANN controller in power system," in *Proc. 1st Int. Conf. Elect. Energy Syst.*, pp. 269–274, Jan. 2011.

[7] R. Dhanalakshmi and S. Palaniswami, "Application of multi stage fuzzy logic control for load frequency control of an isolated wind diesel hybrid power system," in *Proc. Int. Conf. Green Technol. Environmental Conservat.*, pp. 309–315, Dec. 2011.

[8] F. H. Dupont, A. Péres, and S. V. G. Oliveira, "Fuzzy control of a three-phase step-up DC-DC converter with a three-phase high frequency transformer," in *Proc. Brazilian Conf. Power Electron.*, pp. 725–732, Sept. 2009.

[9] R. Sakamoto, T. Senjyu, N. Urasaki, T. Funabashi, H. Fujita, and H. Sekine, "Output power leveling of wind turbine generators using pitch angle control for all operating regions in wind farm," in *Proc. 13th Int. Conf. Intell. Syst. Appl. Power Syst.*, pp. 367–372, Nov. 2005.

[10] T. Goya, E. Omine, Y. Kinjyo, T. Senjyu, A. Yona, N. Urasaki, and T. Funabashi, "Frequency control in isolated island by using parallel operated battery systems applying $\mathcal{H}_\infty$ control theory based on droop characteristics," *IET Renew. Power Gener.*, vol. 5, no. 2, pp. 160–166, Mar. 2011.

[11] V. P. Singh, S. R. Mohanty, N. Kishor, and P. K. Ray, "Robust H-infinity load frequency control in hybrid distributed generation system," *Int. J. Elect. Power Energy Syst.*, vol. 46, pp. 294–305, Mar. 2013.

[12] Q. L. Lam, A. I. Bratcu, D. Riu, and J. Mongkoltanatas, "Multi-variable H-infinity robust control applied to primary frequency regulation in microgrids with large integration of photovoltaic energy source," in *Proc. IEEE Int. Conf. Ind. Technol.*, pp. 2921–2928, Mar. 2015.

[13] Y. Han, A. Jain, P. Young, and D. Zimmerle, "Robust control of microgrid frequency with attached storage system," in *Proc. IEEE 52nd Conf. Decision Control*, pp. 3043–3048, Dec. 2013.

[14] G. Delille, B. François, and G. Malarange, "Dynamic frequency control support by energy storage to reduce the impact of wind and solar generation on isolated power systems inertia," *IEEE Trans. Sustain. Energy*, vol. 3, no. 4, pp. 931–939, Oct. 2012.

[15] P. Thounthong, V. Chunkag, P. Sethakul, S. Sikkabut, S. Pierfederici, and B. Davat, "Energy management of fuel cell/solar cell/supercapacitor hybrid power source," *J. Power Sour.*, vol. 196, no. 1, pp. 313–324, Jan. 2011.

[16] A. Kuperman and I. Aharon, "Battery-ultracapacitor hybrids for pulsed current loads: A review," *Renew. Sustain. Energy Reviews*, vol. 15, no. 2, pp. 981–992, Feb. 2011.

[17] G. M. A. Delille, "Contribution du stockage à la gestion avancée des systèmes électriques, approches organisationnelles et technico-économiques dans les réseaux de distribution," *Ph.D Dissertation, École Centrale de Lille*, Nov. 2010.

[18] P. Kundur, *Power System Stability and Control*, McGraw-Hill, 1994.

[19] D. Maksimovíc, A. M. Stankovíc, V. J. Thottuvelil, and G. C. Verghese, "Modeling and simulation of power electronic converters," *Proc. IEEE*, vol. 89, no. 6, pp. 898–912, Jun. 2001.

[20] A. Yazdani and R. Iravani, *Voltage-Sourced Converters in Power Systems: Modeling, Control, and Applications*. John Wiley & Sons, 2010.

[21] S. Skogestad and I. Postlethwaite, *Multivariable Feedback Control: Analysis and Design*. John Wiley & Sons, 2005.